



Cite this: DOI: 10.1039/d5ea00095e

## Localized pollutant emission increases in China due to COVID-19 lockdowns

Fanghe Zhao, Yuhang Wang\* and Shengjun Xi

Previous studies reported significant decreases in pollutant emissions across industrialized countries during COVID-19 lockdowns in the spring of 2020. However, high-resolution inverse modeling of satellite observations of nitrogen dioxide ( $\text{NO}_2$ ) by the TROPOMI instrument reveals significant increases in nitrogen oxide ( $\text{NO}_x = \text{NO} + \text{NO}_2$ ) emissions in some locations despite widespread reductions in economic activity and mobility due to COVID-19 control measures. The  $\text{NO}_x$  emission increases are associated with supply routes to locked-down cities and urban-to-suburban emission shifts. For example, the total  $\text{NO}_x$  emissions over the Jiang-Han Plain region, where the supply routes to Wuhan were located, increased by 25% during the lockdown. After the lockdown measures were lifted,  $\text{NO}_x$  emissions showed uneven recoveries of economic activities. Significant increases in  $\text{NO}_x$  emissions were observed in the northern part of Jiangsu Province, which has a notable concentration of small-scale or home-based factories, indicating a more rapid resurgence of small enterprises. This research highlights the potential of satellite-based pollutant observations as a valuable tool for assessing socioeconomic activities during pivotal events, such as a pandemic lockdown.

Received 13th August 2025  
Accepted 2nd December 2025

DOI: 10.1039/d5ea00095e  
rsc.li/esatmospheres

### Environmental significance

Previous studies reported large decreases in air pollution during the COVID-19 lockdowns in spring 2020. However, high-resolution satellite observations from TROPOMI show a more complex response for nitrogen oxides ( $\text{NO}_x$ ) in China. Although overall activity declined,  $\text{NO}_x$  emissions increased in specific locations, especially along supply routes to locked-down cities and in suburban areas. For example, emissions over the Jiang-Han Plain, which supplies Wuhan, rose by 25% despite urban reductions. Post-lockdown recovery was uneven, with northern Jiangsu Province experiencing strong rebounds linked to small-scale manufacturing. These findings challenge the assumption that lockdowns uniformly improve air quality and demonstrate how emergency responses can shift emission sources. Satellite observations offer a powerful tool for tracking these changes and informing sustainable crisis management.

## 1. Introduction

The COVID-19 outbreak was first reported in December 2019 in the city of Wuhan, China, and the pandemic had far-reaching impacts on global health, economies, and societies.<sup>1,2</sup> As nations grappled with the rapid transmission and uncertain prognosis of COVID-19, lockdown measures were enforced worldwide, significantly altering societal behaviors and levels of activity.<sup>3</sup> In Wuhan, the epicenter of the initial outbreak, stringent lockdown protocols were initiated as early as January 2020 in an attempt to control viral transmission.<sup>4,5</sup>

The impacts of the lockdown measures and subsequent lifting of these measures were often difficult to quantify. However, the associated changes are reflected in satellite observations of air pollutants. Nitrogen oxides,  $\text{NO}_x$  ( $\text{NO} + \text{NO}_2$ ), are emitted from anthropogenic sources such as transportation, power plants, and industries, contributing significantly to the formation of photochemical smog, acid rain, and ground-level

ozone, thereby affecting air quality, climate change, and human health.<sup>6–8</sup> Prior studies reported drastic reductions in  $\text{NO}_x$  emissions in China during the lockdown due to decreased industrial production and traffic volume.<sup>9–13</sup> However, some areas experienced unexpected surges in  $\text{NO}_x$  emissions during the lockdown period.<sup>14,15</sup>

Prior research primarily focused on broader regional transformations rather than examining in-depth emission variations across urban–suburban areas and highways. Moreover, these studies were predominantly interested in the implications of emission reductions due to the COVID-19 pandemic. In contrast, this study employs a high-resolution inversion technique to scrutinize the nuanced details of emission changes. It specifically focuses on the emission enhancements resulting from changes in the supply chain and human activities. An in-depth investigation into this paradoxical phenomenon provides critical insights into the complex interactions between human activities and environmental emissions, a subject that is particularly relevant under unprecedented circumstances such as a pandemic lockdown.

School of Earth and Atmospheric Sciences, Georgia Institute of Technology, Atlanta, GA 30332, USA. E-mail: yuhang.wang@eas.gatech.edu



Our study advances this field by implementing a 4 km resolution inversion analysis of  $\text{NO}_x$  emissions using the state-of-the-art 3D Regional Chemical Transport Model (REAM) and TROPOMI satellite observations. Through this high-resolution approach, we identify specific regions in China where  $\text{NO}_x$  emissions increased during the lockdown, attributing these changes to essential activities such as makeshift hospital construction, emergency goods transportation, and regional support for major cities. Furthermore, we document the uneven post-lockdown recovery in emissions, highlighting distinct regional patterns in the pace and nature of economic resumption.

This investigation examines emission changes across diverse regions in China by dividing East China: the Jiang-Han Plain covering Wuhan city and surrounding areas (Region I), Nanjing-Hefei Area (Region II), and Yangtze River Delta (Region III). This division enables detailed analysis of how COVID-19 lockdown policies impacted these three major populated regions and their distinct behavioural patterns during both lockdown and recovery phases. We analyzed these changes across three distinct temporal phases following:<sup>11</sup> pre-lockdown (January 1–23, 2020) representing the pre-lockdown period, Phase I (January 23–February 20, 2020) corresponding to the main lockdown period, and Phase II marking the initial recovery period in China.

Our research contributes to understanding how global crises like the COVID-19 pandemic influence environmental conditions at local scales. The high-resolution analysis provides crucial insights for developing targeted strategies to mitigate environmental impacts during future crises. These findings will benefit policymakers, environmental scientists, and stakeholders across industry and public health sectors by providing quantitative evidence of how emergency measures affect regional air quality and economic activities.

The remainder of this paper is organized as follows: Section 2 details our methodology, including the REAM model configuration and TROPOMI data processing protocols. Section 3 presents our analysis of regional emission changes during the lockdown period and evaluates post-lockdown recovery patterns across the three subregions. Section 4 summarizes our findings and discusses their implications for future research and policy development, particularly in the context of emergency response planning and environmental protection.

## 2. Methods

### 2.1 Observation

**2.1.1 TROPOMI  $\text{NO}_2$  measurements.** We utilized the  $\text{NO}_2$  observations from TROPOMI aboard Sentinel-5P. TROPOMI offers significantly improved spatial resolution compared to OMI,<sup>16</sup> with  $5.6 \times 3.6 \text{ km}^2$  resolution at nadir (following the August 2019 update), approximately ten times finer than OMI's  $13 \times 24 \text{ km}^2$ . The instrument operates in sun-synchronous orbit with 13:30 local time equatorial crossing, providing daily global coverage *via* its 2600 km swath.<sup>17</sup> This enhanced resolution enables more accurate detection of  $\text{NO}_2$  spatial gradients and better source separation in Chinese megacities, making it

particularly suitable for urban-scale studies during the COVID-19 lockdown period.

The KNMI  $\text{NO}_2$  retrieval algorithm for TROPOMI builds upon the established DOMINO retrieval system, incorporating several methodological improvements. The algorithm employs differential optical absorption spectroscopy (DOAS) to determine the total  $\text{NO}_2$  slant column density, which is then separated into stratospheric and tropospheric components using data assimilation techniques.<sup>18,19</sup> These components are converted to vertical column densities through altitude-dependent air mass factors, utilizing  $\text{NO}_2$  vertical profiles from the TM5-MP model and surface albedo information from monthly OMI climatology. For this study, we use the offline (OFFL) level 2 v1.2  $\text{NO}_2$  product, applying a cloud radiative fraction threshold of 0.3 to filter cloudy pixels.<sup>20</sup> Validation studies over major Chinese cities demonstrate that TROPOMI provides more reliable  $\text{NO}_2$  retrievals compared to OMI, particularly in highly polluted urban areas where OMI often suffered from saturation effects and coarse spatial resolution.<sup>9,21–23</sup>

**2.1.2 CNEMC data.** Surface  $\text{O}_3$  concentrations from the China National Environmental Monitoring Centre (CNEMC) network provided independent validation.<sup>24</sup> The network comprises over 1500 urban and suburban stations measuring criteria pollutants. We selected stations within our study domains (Hubei, Nanjing-Hefei, and Yangtze River Delta regions) and extracted hourly measurements coincident with TROPOMI overpasses (12:00–14:00 local time). Quality control procedures included outlier removal and diagnostic flag screening.<sup>25</sup> We chose  $\text{O}_3$  rather than direct  $\text{NO}_2$  measurements because surface  $\text{O}_3$  formation is tightly coupled to  $\text{NO}_x$  emissions through photochemical pathways, providing a robust indicator of both emission magnitudes and chemical transformation accuracy. Additionally, previous studies have documented systematic overestimation biases in  $\text{NO}_2$  measurements using molybdenum oxide converters,<sup>26–28</sup> making  $\text{O}_3$  a more reliable validation metric for high-pollution environments in China.

### 2.2 Models

**2.2.1 Regional chemical and transport model (REAM).** We employed the Regional chEmical and trAnsport Model (REAM), which has been extensively validated through numerous applications including emission inversions, ozone simulations, and mechanistic studies of atmospheric processes.<sup>27,29–35</sup> Our model configuration consists of a nested domain structure with an outer grid horizontal resolution of  $12 \times 12 \text{ km}$  and an inner grid horizontal resolution of  $4 \times 4 \text{ km}$ , incorporating 30 vertical layers in the troposphere, the domain information is shown in SI Fig. S1. The model's chemical mechanism is based on GEOS-Chem v11.01 with updated aromatics reactions from SAPRC07, while meteorological fields are provided by the Weather Research and Forecasting (WRF v4.0) model with data nudging using ECMWF Reanalysis v5.<sup>36</sup> The outer domain utilizes anthropogenic emissions from the Multi-resolution Emission Inventory for China (MEIC) 2017,<sup>37</sup> while the inner domain emissions are initially based on MEIC 2017 and subsequently



optimized through top-down inversion. Chemical boundary conditions for the outer domain are derived from GEOS-Chem ( $2^\circ \times 2.5^\circ$ ) simulations, while the inner nested grid receives boundary conditions from the outer grid, ensuring consistent chemical transport across domain boundaries.

**2.2.2 Inverse modeling.** Inverse modeling is a robust tool in atmospheric research, facilitating the derivation of nitrogen oxide ( $\text{NO}_x$ ) emissions from satellite measurements. This process exploits the high-resolution data gathered by satellite instruments, such as the Ozone Monitoring Instrument (OMI) and the Tropospheric Monitoring Instrument (Tropomi). The technique involves using algorithms that transform satellite-observed concentrations of  $\text{NO}_x$  into emission estimates, which can then be integrated into air quality simulations and global chemical data assimilation models.<sup>27,28,38-41</sup> Previous studies also used the  $\text{NO}_x$  inverse modeling to comprehensively understand emission changes, infer economic development, and guide pollution control policies.<sup>42,43</sup> Gu *et al.* (2013, 2014), for example, showed that the annual increase in anthropogenic  $\text{NO}_x$  emissions in China from 1996–2006 was  $4.01 \pm 1.39\%$  per year, a significant slowdown from prior estimates, with cooler seasons and less economically developed regions showing higher growth rates and revealed higher emissions in winter and summer than in spring (and possibly fall), and an increasing weekday-to-weekend emission ratio correlated with  $\text{NO}_x$  emission magnitude.

We implemented an advanced Bayesian  $\text{NO}_x$  emission inversion framework, building upon methodologies established by ref. 42, while incorporating significant improvements in spatial resolution. The inversion system processes daily Tropomi observations from January 1 to March 30, 2020, coinciding with the satellite's early afternoon overpass time (approximately 13:30 local time).

Our inversion framework employs a sophisticated top-down approach in which  $\text{NO}_x$  emissions are optimized by comparing Tropomi-observed tropospheric  $\text{NO}_2$  columns with REAM model simulations. The optimization utilizes a comprehensive error-weighted scheme that carefully balances observation errors, *a priori* emission uncertainties, and model representation errors. We quantified the posteriori uncertainties in our emission estimates by combining three independent error sources through error propagation analysis. Following established protocols,<sup>43,44</sup> we assigned a 25% uncertainty to account for the model representation error. We then propagated model and Tropomi measurement uncertainties<sup>45</sup> as independent sources to derive the total fractional uncertainty. The final absolute uncertainty,  $E_\varepsilon$ , in estimated emissions, was calculated by applying this total fractional uncertainty to the posterior emission magnitude:

$$E_\varepsilon = E_{\text{posterior}} \times (\varepsilon_{\text{TropOMI}}^2 + 0.25^2)^{1/2}$$

where  $\varepsilon_{\text{TropOMI}}$  denotes TropOMI retrieved tropospheric column  $\text{NO}_2$  relative uncertainty.

Our inversion employed a sequential daily optimization approach<sup>46</sup> designed to track rapid emission changes during the COVID-19 lockdown period. Each day's optimized emissions

and associated uncertainties served as prior information for the subsequent day's calculations, creating a dynamic updating mechanism. We calculated air mass factors using REAM vertical profiles and WRF meteorological data to derive satellite tropospheric  $\text{NO}_2$  vertical column densities (VCDs). The posterior  $\text{NO}_x$  emissions were then determined by scaling the prior emissions based on the ratio between satellite-retrieved and 3D REAM-simulated  $\text{NO}_2$  VCDs. These updated emissions were fed back into REAM to recalculate air mass factors and perform the next iteration of retrieval and inversion.

To ensure data quality, we implemented enhanced screening procedures, including cloud filtering with a threshold of 0.3 cloud fraction. As documented in validation studies over major Chinese cities, Tropomi provides reliable  $\text{NO}_2$  retrievals in eastern China's high-pollution environments, with its improved spatial resolution and sensitivity addressing limitations observed in previous satellite instruments such as OMI. The detailed schematic of this inversion methodology is illustrated in SI Fig. S2. This refined methodology enables better quantification of  $\text{NO}_x$  emission changes at unprecedented spatial resolution (4 km), making it particularly suitable for analyzing the complex emission patterns that emerged during the COVID-19 lockdown and subsequent recovery periods.

### 2.3 Study region selection and justification

The selection of our three study regions was designed to capture diverse impacts of COVID-19 lockdown measures across eastern China. Region I (Jiang-Han Plain) encompasses Wuhan and surrounding areas that experienced China's strictest lockdown from January 23 to April 8, 2020,<sup>11</sup> representing a unique case where stringent movement restrictions coincided with intensive humanitarian logistics operations. Region II (Nanjing–Hefei Area) represents a mixed urban-industrial corridor with diverse industrial structures ranging from large state-owned enterprises to small-scale manufacturing, enabling analysis of differential lockdown impacts across various enterprise scales.<sup>47</sup> Region III (Yangtze River Delta) is China's most economically developed region and a major export-oriented manufacturing hub, allowing examination of how global supply chain pressures influenced emission patterns during and after lockdown.<sup>48</sup> Together, these regions encompass substantial variation in economic development, industrial structures, and lockdown stringency, ensuring our findings capture the full spectrum of emission responses to pandemic control measures.

## 3. Results

### 3.1 $\text{NO}_x$ emission changes for the three regions

The implementation of COVID-19 lockdown policies on January 23, 2020, resulted in substantial decreases in  $\text{NO}_x$  emissions across all three study domains (Fig. 1). Overall,  $\text{NO}_x$  emissions declined by approximately 35% across the entire study region. Region-specific analysis revealed heterogeneous reduction patterns: Whole Region I (Hubei Area) showed a 12% decrease, Region II (Hefei–Nanjing Area) experienced the most substantial reduction at 45%, and Region III (Yangtze River Delta Area)





**Fig. 1** Temporal evolution of NO<sub>x</sub> emissions during the COVID-19 outbreaks. Daily NO<sub>x</sub> emissions from January to March 2020 for (a) all domains, (b) Region I: Hubei Province, (c) Region II: Hefei–Nanjing Area, and (d) Region III: Yangtze River Delta. Background shading indicates pre-lockdown (yellow), Phase I lockdown (orange), and Phase II recovery (green) periods. Red and green vertical lines mark lockdown initiation (23 January) and relaxation (20 February), respectively. Error bars show daily inversion uncertainties.

exhibited a 15% decrease. Given our model uncertainty, the difference between Hubei (12%) and Yangtze River Delta (15%) falls within the uncertainty bounds and should not be interpreted as statistically significant. However, the magnitude of reduction in Region II (45%) represents a clearly distinct response, exceeding the reductions in both Regions I and III by more than twice the combined uncertainties. While the NO<sub>x</sub> emission reductions in Hubei (12%) and Yangtze River Delta (15%) are statistically indistinguishable within our uncertainty bounds, both regions showed markedly smaller reductions than Region II (45%). The relatively modest reduction in Hubei is particularly notable given that it contained Wuhan, the epicenter with the strictest lockdown measures. This apparent paradox is likely attributable to two main factors. First, emission reductions were concentrated in urban centers, and Hubei has a lower density of large cities than the other regions. For example, the emission decrease in Wuhan was 42%, substantially higher than the regional average of 12%. Second, the complete shutdown of Wuhan required logistical support from surrounding areas, potentially leading to increased emissions in those regions. We examine these factors in greater detail in the next section. The effect of population movement away from Wuhan for fear of the COVID-19 outbreak is another factor that partially offset the urban reductions.

Following the initial easing of lockdown measures (Phase II), NO<sub>x</sub> emissions displayed region-specific responses. In Region I, emissions continued to decline, primarily due to prolonged restrictions in Wuhan, the epicenter of the outbreak. Conversely, Region II experienced a notable increase in emissions, attributable to intensified goods transportation activities.<sup>49</sup> Region III showed a slight increase before stabilizing.

The observed emission changes must be interpreted considering that our baseline period (January 1–23, 2020)

coincides with the Chunyun travel rush period preceding Spring Festival 2020 (January 25). During Chunyun, which typically begins two weeks before Spring Festival, industrial NO<sub>x</sub> emissions decrease substantially as factories reduce operations and workers migrate to their hometowns. The satellite-derived NO<sub>x</sub> emission time series do not exhibit a significant decline from January 1 to 23 (Fig. 1), suggesting that increased transportation-related emissions more than offset the reductions from industrial activities leading up to the Spring Festival in the study regions.

Satellite observations during Spring Festival periods have documented significant reductions in tropospheric NO<sub>2</sub> column density, with decreases in megacities ranging from 32% to 45%, primarily attributed to reduced industrial activity and transportation during the holiday period.<sup>50,51</sup> Emission reductions show a sharp decline around the Spring Festival period with cities experiencing reductions of 20–50%.<sup>52</sup> Therefore, the 35% overall emission decrease we observed during Phase I likely represents a modest reduction beyond typical Spring Festival decreases.

### 3.2 NO<sub>x</sub> emission distribution change during the COVID lockdown

**3.2.1 Urban–suburban emission dynamics.** High-resolution analysis revealed that NO<sub>x</sub> emission reductions were not spatially uniform but exhibited complex redistribution patterns, which were related strongly to changes in anthropogenic activities (Fig. 2). Metropolitan areas experienced pronounced decreases in emissions, while many suburban and rural areas showed contrasting patterns of increased emissions, reflecting significant shifts in economic activities and population movement away from urban areas during lockdown.

Regional NO<sub>x</sub> emission patterns during the lockdown period revealed contrasting trends between major urban centres and smaller cities in the Hefei–Nanjing region. SI Fig. S3 shows time series data for three distinct subregions within the Hefei–

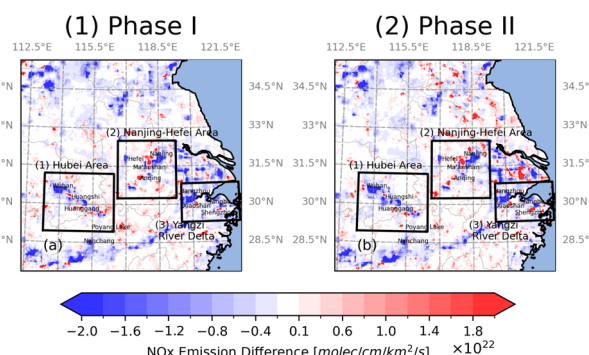


**Fig. 2** Spatial distribution of NO<sub>x</sub> emission differences between lockdown phases and pre-lockdown baseline over eastern China. (a) Phase I (strict lockdown) and (b) Phase II (early recovery) emission changes. Black boxes denote three study regions: (1) Region I: Hubei Area, (2) Region II: Nanjing–Hefei Area, and (3) Region III: Yangtze River Delta. Negative values (blue) indicate emission reductions; positive values (red) indicate increases.



Nanjing metropolitan area. Fig. 3 illustrates the spatial distributions of emission differences between each lockdown phase and the pre-lockdown baseline for the Hefei–Nanjing region. While the metropolitan areas of Hefei and Nanjing experienced significant  $\text{NO}_x$  emission reductions, smaller cities including Ma'anshan and Anqing paradoxically showed increased emissions (Fig. 3). This spatial heterogeneity likely reflects population redistribution during the lockdown, with workers migrating from major urban centres to their hometowns and residents relocating to suburban areas, effectively transferring emission sources from large to small cities.<sup>53,54</sup>

This pattern of emission redistribution extended beyond the Hefei–Nanjing region to the Yangtze River Delta region. SI Fig. S4 presents time series data for three distinct subregions within the Yangtze River Delta. Fig. 4 illustrates the spatial distributions of emission differences between each lockdown phase and the pre-lockdown baseline for the Yangtze River Delta region. Similar urban-to-suburban transfer dynamics emerged. Hangzhou—a major technology hub—demonstrated substantial emission reductions (50%) during the lockdown period, primarily attributable to widespread remote work adoption among technology sector employees.<sup>55–57</sup> Consistent with the pattern observed in the Hefei–Nanjing region, this urban reduction coincided with a notable increase in  $\text{NO}_x$  emissions in the adjacent Xiaoshan region, where many urban workers relocated during the work-from-home mandate.<sup>56</sup> These similar urban–suburban emission dynamics emerged across other major regions. Shanghai, one of the world's most densely populated urban areas, likewise exhibited consistent decreases in  $\text{NO}_x$  emissions throughout both Phase I and Phase II of the lockdown,<sup>58,59</sup> further exemplifying the complex redistribution of emissions as urban activities shifted to suburban residential areas during the pandemic response.

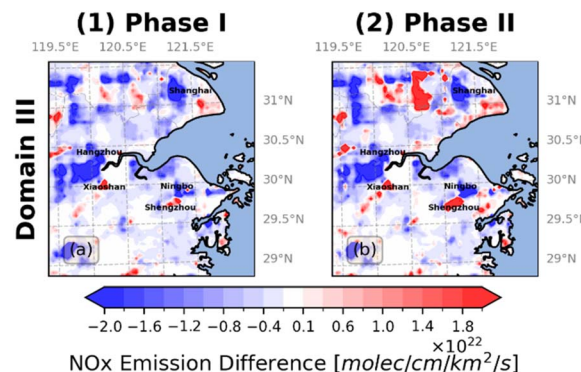


Fig. 4 High-resolution  $\text{NO}_x$  emission changes across study domains during COVID-19 lockdown phases relative to pre-lockdown baseline. Spatial distribution of  $\text{NO}_x$  emission differences ( $\times 10^{22}$  molecules  $\text{cm}^{-2} \text{ km}^{-2} \text{ s}^{-1}$ ) for (a) Phase I (lockdown period, left column) and (b) Phase II (recovery period, right column) compared to pre-lockdown levels across Domain III (Yangtze River Delta). Blue colors indicate emission decreases while red colors represent emission increases relative to baseline conditions. Major cities are labelled within each domain.

Regionally, the about 45% decrease over the Hefei–Nanjing corridor exceeds that over the core Yangtze River Delta (YRD). Prior studies report large but regionally varying  $\text{NO}_x$  emission reductions during the early-2020 lockdown, including a peak reduction in the YRD on the order of 41%, and an average 30% reduction over eastern China.<sup>60</sup> Population mobility data shows that movements dropped sharply after the Lunar New Year and remained suppressed into mid-February, indicating a delayed workforce return that is consistent with stronger inland activity declines.<sup>61</sup> At the same time, research on port operations and liner-shipping networks documented a substantial disruption but also continuity and early reconfiguration in major Chinese and Asian ports, helping explain comparatively sustained coastal logistics activity near the YRD.<sup>62,63</sup> City-scale analyses for Nanjing report pronounced  $\text{NO}_2$  decreases during lockdown, consistent with the stronger inland reduction we infer for the Hefei–Nanjing corridor.<sup>64</sup>

Jiangsu Province accounts for one-eighth of national manufacturing production and is home to numerous small-scale and home-based factories.<sup>65–67</sup> Compared to other regions, this region exhibited the most pronounced  $\text{NO}_x$  emission rebound relative to pre-COVID levels. Within Jiangsu, cities with distinct industrial profiles showed varying recovery patterns (Fig. 5). Wuxi and Suzhou, recognized for their labor-intensive small-scale manufacturing and furniture industries,<sup>67–69</sup> experienced  $\text{NO}_x$  emission rebounds of 27% above pre-COVID baselines after lockdown. Similarly, Huai'an, known for kitchenware and sportswear production,<sup>67–69</sup> demonstrated a 186% increase in  $\text{NO}_x$  emissions compared to pre-pandemic levels after the lockdown. The particularly strong recovery in these export-oriented manufacturing centres likely reflects intensified production efforts to fulfill accumulated international orders following the lifting of initial lockdown restrictions.<sup>70–72</sup>

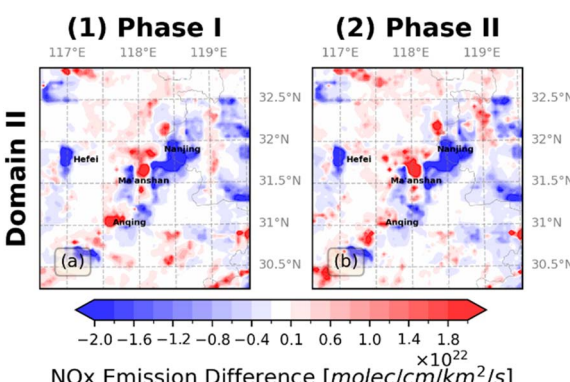


Fig. 3 High-resolution  $\text{NO}_x$  emission changes across study domains during COVID-19 lockdown phases relative to pre-lockdown baseline. Spatial distribution of  $\text{NO}_x$  emission differences ( $\times 10^{22}$  molecules  $\text{cm}^{-2} \text{ km}^{-2} \text{ s}^{-1}$ ) for (a) Phase I (lockdown period, left column) and (b) Phase II (recovery period, right column) compared to pre-lockdown levels across Domain II (Hefei–Nanjing Area). Blue colors indicate emission decreases while red colors represent emission increases relative to baseline conditions. Major cities are labeled within each domain.



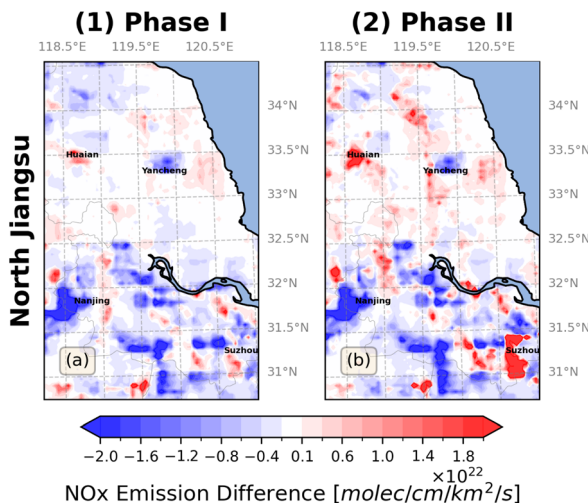


Fig. 5 High-resolution NO<sub>x</sub> emission changes across North Jiangsu during COVID-19 lockdown phases relative to pre-lockdown baseline. Spatial distribution of NO<sub>x</sub> emission differences ( $\times 10^{22}$  molecules  $\text{cm}^{-2} \text{ km}^{-2} \text{ s}^{-1}$ ) for (a) Phase I (lockdown period, left column) and (b) Phase II (recovery period, right column) compared to pre-lockdown levels across Poyang Lake Staging Area. Blue colors indicate emission decreases while red colors represent emission increases relative to baseline conditions.

The 186% emission increase observed in Huai'an during Phase II requires careful interpretation within the Spring Festival context. Phase II (February 21–March 1) corresponds to the post-festival period when factories resume operations and workers return to cities. Our baseline period (January 1–23, 2020) coincided with the Chunyun travel rush and Spring Festival preparations, when emission reductions may occur due to factory shutdowns and worker migration. Studies using machine learning to decouple meteorological effects from emission changes have documented that Spring Festival typically causes varied NO<sub>2</sub> reductions in Chinese cities. Dai *et al.* found a 14.1% decrease in NO<sub>2</sub> concentrations in major Chinese cities during 2015–2019,<sup>73</sup> while Li *et al.* reported that megacities showed reductions in tropospheric NO<sub>2</sub> column density ranging from 31.8% to 44.5%.<sup>50</sup>

The interaction between Spring Festival timing and lockdown measures creates complexity in interpreting our emission changes. After accounting for meteorological effects and Spring Festival patterns, lockdown-attributable NO<sub>2</sub> reductions in Chinese cities averaged 15.4%, considerably smaller than the combined effect when Spring Festival patterns are not decoupled.<sup>73</sup> This suggests that our observed 35% overall emission decrease during Phase I likely includes both lockdown and Spring Festival effects. Conversely, the emission increases we detected in Poyang Lake region (259%), which are much higher than in Jiang-Han Plain (25%), making these increases even more notable as indicators of exceptional logistics and manufacturing activities.

The magnitude of spatial variation in our observed changes (from -45% to +259%) substantially exceeds typical emission fluctuations documented in previous Spring Festival studies,

where reductions in megacities ranged from 31.8% to 44.5%.<sup>50</sup> This much expanded range of changes confirms that lockdown-specific factors, particularly emergency logistics operations and localized manufacturing intensification, dominated over seasonal patterns in determining the spatial distribution of emission changes during early 2020.

**3.2.2 Emission increases in logistics support regions.** Our analysis also identified significant NO<sub>x</sub> emission increases associated with humanitarian support activities for Wuhan during Phase I. SI Fig. S5 presents time series data for three distinct subregions within the Jianghan Plain. Fig. 6 illustrates the emission differences between each lockdown phase and the pre-lockdown baseline for the Jianghan Plain region. These emission increases manifested along key transportation networks, near medical infrastructure development sites, and across logistical staging areas.

Major transportation arteries, particularly G70 Fuyin Expressway, showed marked increases in NO<sub>x</sub> emissions during Phase I (Fig. 6). These elevated emissions directly reflected the intensive movement of medical supplies, equipment, and healthcare personnel, along with the continuous delivery of essential goods to support locked-down areas. The increased traffic flow along these crucial corridors highlighted their vital role in maintaining supply chains during the crisis.<sup>74–76</sup> The total NO<sub>x</sub> emissions over the Jiang-Han Plain region increased by 25% during the lockdown.

The city of Huanggang emerged as a significant point of increased emissions due to the rapid development and operation of temporary medical facilities<sup>76,77</sup> (Fig. 6). The construction and operation of these facilities necessitated enhanced logistics activities and increased movement of healthcare workers and support staff, contributing to elevated NO<sub>x</sub> emissions in the region. This localized increase underscores the environmental impact of emergency medical infrastructure development during crisis responses.<sup>78</sup> Huanggang NO<sub>x</sub> emissions increased by 248% from the pre-lockdown baseline period.

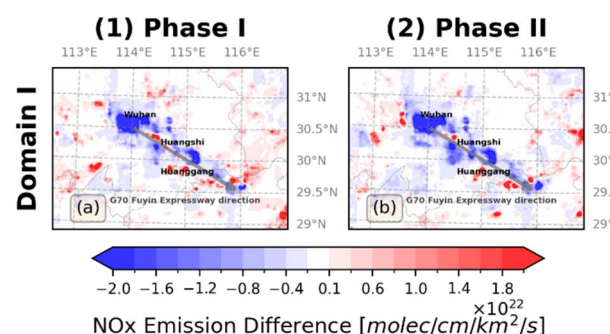


Fig. 6 High-resolution NO<sub>x</sub> emission changes across study domains during COVID-19 lockdown phases relative to pre-lockdown baseline. Spatial distribution of NO<sub>x</sub> emission differences ( $\times 10^{22}$  molecules  $\text{cm}^{-2} \text{ km}^{-2} \text{ s}^{-1}$ ) for (a) Phase I (lockdown period, left column) and (b) Phase II (recovery period, right column) compared to pre-lockdown levels for Domain I (Hubei Area). Blue colors indicate emission decreases while red colors represent emission increases relative to baseline conditions. Major cities are labeled within each domain.



The Poyang Lake region also showed an unexpected but significant increase in  $\text{NO}_x$  emissions (Fig. 7), serving as a crucial logistics hub in the emergency response network. This area functioned as a strategic staging ground for supplies originating from the Nanjing–Hefei region and Nanchang city, facilitating the temporary storage and redistribution of medical and essential supplies to support Wuhan.<sup>79–81</sup> The increased emissions in this region reflect the intensified activities associated with its role as a critical connection point in the emergency supply chain.  $\text{NO}_x$  emissions from the Poyang Lake region increased by 259% during the Phase I period compared to the pre-lockdown baseline period.

These findings reveal the complex environmental implications of emergency response measures during the pandemic. The observed increases in  $\text{NO}_x$  emissions in logistics support zones demonstrate how large-scale humanitarian operations can create unexpected environmental impacts, even as they fulfil crucial public health needs. The spatial distribution of these emission changes provides valuable insights into the relationship between human mobility patterns, economic activities, and environmental impacts during crisis periods, offering important lessons for future public health emergency responses. The varying patterns of  $\text{NO}_x$  emissions derived from satellite observations across different regions and logistics support zones highlight the intricate interplay between emergency response measures and environmental impacts, which can inform more effective and environmentally conscious approaches to crisis management while maintaining the capability to respond rapidly to public health emergencies. Understanding these patterns is crucial for developing policies that can better balance immediate emergency needs with longer-term environmental considerations in future crisis scenarios.

### 3.3 Ground-based validation of emission patterns

To strengthen our analysis of satellite-derived emission changes, we synthesize findings from previously published

studies on ground-based activity indicators during the COVID-19 lockdown period. The convergence of evidence from multiple independent data sources validate our satellite-based observations and sheds light on the underlying processes that generated the observed emission patterns.

#### 3.3.1 Activity indicators and spatial redistribution.

Multiple ground-based data sources documented the dramatic activity changes that drove the emission change patterns we observed. China's Ministry of Transport reported that total passenger volume across all transport modes dropped 50.9% during January–February 2020, while freight volume declined only 19.7%,<sup>82</sup> underscoring the essential role of supply chains despite restrictions on passenger movement. Detailed analysis showed long-haul trucking volumes fell below 15% of 2019 levels between January 24 and February 26, 2020, but rebounded quickly to 50% by late February and 92% by March.<sup>83</sup> This recovery timeline closely matches the emission rebound we observed along transportation corridors. Regional analysis confirmed that Wuhan's highway freight transport dropped approximately 90%, while other cities maintained relatively high freight activity,<sup>84</sup> consistent with our spatially resolved emission observations showing persistent hotspots along key supply routes despite urban emission reductions.

Population mobility data from the Baidu migration index platform, which tracks movements of hundreds of millions of mobile phone users, revealed that approximately 20.2 million at-risk population movements occurred from Wuhan between January 1–31, 2020, with 84.5% within Hubei Province.<sup>85,86</sup> Following the January 25 national emergency response, analysis of 358 Chinese cities showed intra-city movement intensity decreased substantially, with mobility falling by as much as 80% compared to normal days and by 58% compared to the same lunar period in 2019.<sup>87,88</sup> Notably, mobility data documented substantial urban-to-suburban population redistribution as residents temporarily relocated or adopted remote work arrangements,<sup>88</sup> directly accounting for the suburban emission increases we observed in our satellite data. Quantitative analysis further demonstrated that daily COVID-19 infection cases correlated significantly with local mobility ( $R^2 = 0.77$ ), and the reproduction number declined by 3% for every 10% reduction in mobility,<sup>87,89,90</sup> establishing the close link between movement restrictions, disease control, and emission changes.

Electricity consumption served as a real-time proxy for industrial activity. China's national electricity consumption in Q1 2020 declined 6.5% year-over-year, a dramatic reversal from the 5.5% increase in Q1 2019.<sup>91</sup> The secondary (industrial) sector experienced approximately 14% consumption decrease in February 2020, while residential consumption increased modestly by 6.6% and 4.5% in Q1 and Q2, respectively, due to stay-at-home measures.<sup>92,93</sup> Regionally, Hubei Province experienced the largest declines, exceeding 20% during January–February, while coastal provinces reported smaller reductions.<sup>92,94</sup> Analysis of multiple industries revealed heterogeneous impacts even within sectors, with some firms maintaining production for essential goods or export commitments.<sup>95</sup> By April 2020, consumption began recovering, with weather-corrected demand exceeding 2019 levels by August in

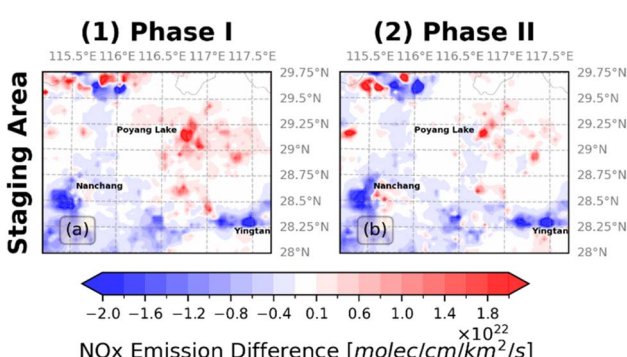


Fig. 7 High-resolution  $\text{NO}_x$  emission changes across Staging Area during COVID-19 lockdown phases relative to pre-lockdown baseline. Spatial distribution of  $\text{NO}_x$  emission differences ( $\times 10^{22}$  molecules  $\text{cm}^{-2} \text{ km}^{-2} \text{ s}^{-1}$ ) for (a) Phase I (lockdown period, left column) and (b) Phase II (recovery period, right column) compared to pre-lockdown levels across Poyang Lake Staging Area. Blue colors indicate emission decreases while red colors represent emission increases relative to baseline conditions. Major cities are labeled within each domain.



many regions,<sup>94</sup> mirroring the rapid emission recovery we observed during Phase II.

**3.3.2 Validation of satellite-derived emissions.** Our satellite-derived emission estimates show good quantitative agreement with independent measurements. Studies using surface air quality monitoring networks combined with inverse modeling reported nationwide NO<sub>x</sub> emission reductions of approximately 36% during peak lockdown,<sup>96,97</sup> closely matching our satellite-based estimates. These studies found even larger reductions in major cities, with reductions of 40–70% observed in Wuhan (61%), Shenzhen (65%), Guangzhou (68%), and Harbin (66%),<sup>97</sup> corroborating our observation of severe urban emission reductions under stringent lockdown measures.

Both satellite and ground-based platforms revealed consistent temporal variations: sharp reductions in late January, lowest emissions in mid-February, and gradual recovery from late February through March 2020.<sup>94,96</sup> Hubei Province remained an exception, with extended restrictions until April 8, consistent with our Phase I findings. This temporal synchronization across satellite remote sensing, surface networks, and activity proxies like electricity consumption strongly supports that these patterns reflects real emission changes rather than measurement artifacts.

## 4. Conclusions

Satellite-derived NO<sub>x</sub> emissions at high spatial resolution reveal that societal disruptions trigger complex environmental responses. These responses transcend simple reduction narratives. The COVID-19 lockdown in China created distinctive NO<sub>x</sub> emission signatures that effectively trace human adaptation to crisis conditions, with significant emission increases in suburban areas, logistics hubs, and along key transportation corridors providing insights into population redistribution patterns and humanitarian response operations that would otherwise remain undetected through conventional monitoring approaches.

The observed spatial redistribution of emissions highlights an important trade-off between centralized urban emission reductions and the environmental consequences of decentralized activities, challenging conventional emergency response frameworks that may overlook the environmental implications of humanitarian logistics. Future research should explore the integration of satellite-based high-resolution emission monitoring into emergency management systems and develop capabilities to distinguish between different NO<sub>x</sub> emission sources in near real-time. Such advances could potentially transform how societies balance immediate humanitarian needs with environmental priorities during crisis situations.

## Author contributions

Conceptualization, F. Z. and Y. W.; methodology, F. Z.; software, F. Z.; validation, F. Z. and S. X.; formal analysis, F. Z.; investigation, F. Z.; resources, Y. W.; data curation, F. Z.; writing – original draft preparation, F. Z.; writing – review and editing, F. Z., Y. W. and S. X.; visualization, F. Z.; supervision, Y. W.; project

administration, Y. W.; funding acquisition, Y. W. All authors have read and agreed to the published version of the manuscript.

## Conflicts of interest

There are no conflicts to declare.

## Data availability

TropOMI NO<sub>2</sub> level 2 production from the KNMI is downloaded from <https://www.temis.nl/>. The MEIC emission inventory can be downloaded from <http://meicmodel.org.cn/>. The CNEMC data used in this paper can be downloaded from <https://doi.org/10.6084/m9.figshare.c.7976543.v1>.

Supplementary information (SI): additional supporting figures and a detailed description of the inversion model architecture. See DOI: <https://doi.org/10.1039/d5ea00095e>.

## Acknowledgements

This work was supported in part by the National Science Foundation under Grant No. 2030425. We would also like to acknowledge high-performance computing support from the Derecho system (<https://doi.org/10.5065/qx9a-pg09>) provided by the NSF National Center for Atmospheric Research (NCAR), sponsored by the National Science Foundation. We acknowledge the free use of the TROPOMI NO<sub>2</sub> column data provided through the Sentinel-5 Precursor mission of the European Space Agency (ESA) from <https://www.temis.nl>. The TROPOMI NO<sub>2</sub> level 2 products were processed by the Royal Netherlands Meteorological Institute (KNMI).

## References

- 1 P. Zhou, X.-L. Yang, X.-G. Wang, B. Hu, L. Zhang, W. Zhang, H.-R. Si, Y. Zhu, B. Li, C.-L. Huang, H.-D. Chen, J. Chen, Y. Luo, H. Guo, R.-D. Jiang, M.-Q. Liu, Y. Chen, X.-R. Shen, X. Wang, X.-S. Zheng, K. Zhao, Q.-J. Chen, F. Deng, L.-L. Liu, B. Yan, F.-X. Zhan, Y.-Y. Wang, G.-F. Xiao and Z.-L. Shi, *Nature*, 2020, **579**, 270–273.
- 2 Q. Li, X. Guan, P. Wu, X. Wang, L. Zhou, Y. Tong, R. Ren, S. M. Leung Kathy, H. Y. Lau Eric, Y. Wong Jessica, X. Xing, N. Xiang, Y. Wu, C. Li, Q. Chen, D. Li, T. Liu, J. Zhao, M. Liu, W. Tu, C. Chen, L. Jin, R. Yang, Q. Wang, S. Zhou, R. Wang, H. Liu, Y. Luo, Y. Liu, G. Shao, H. Li, Z. Tao, Y. Yang, Z. Deng, B. Liu, Z. Ma, Y. Zhang, G. Shi, T. Y. Lam Tommy, T. Wu Joseph, F. Gao George, J. Cowling Benjamin, B. Yang, M. Leung Gabriel and Z. Feng, *N. Engl. J. Med.*, 2020, **382**, 1199–1207.
- 3 M. Chinazzi, J. T. Davis, M. Ajelli, C. Gioannini, M. Litvinova, S. Merler, A. Pastore y Piontti, K. Mu, L. Rossi, K. Sun, C. Viboud, X. Xiong, H. Yu, M. E. Halloran, I. M. Longini and A. Vespignani, *Science*, 2020, **368**, 395–400.
- 4 H. Tian, Y. Liu, Y. Li, C.-H. Wu, B. Chen, M. U. G. Kraemer, B. Li, J. Cai, B. Xu, Q. Yang, B. Wang, P. Yang, Y. Cui, Y. Song,



P. Zheng, Q. Wang, O. N. Bjornstad, R. Yang, B. T. Grenfell, O. G. Pybus and C. Dye, *Science*, 2020, **368**, 638–642.

5 H. Lau, V. Khosrawipour, P. Kocbach, A. Mikolajczyk, H. Ichii, J. Schubert, J. Bania and T. Khosrawipour, *J. Microbiol. Immunol. Infect.*, 2020, **53**, 454–458.

6 D. J. Jacob, J. A. Logan and P. P. Murti, *Geophys. Res. Lett.*, 1999, **26**, 2175–2178.

7 H. Qu, Y. Wang, R. Zhang and J. Li, *J. Geophys. Res.: Atmos.*, 2020, **125**, e2020JD033670.

8 J. H. Seinfeld and S. N. Pandis, *Atmospheric Chemistry and Physics: From Air Pollution to Climate Change*, John Wiley & Sons, Hoboken, 2016.

9 C. Wang, T. Wang, P. Wang and V. Rakitin, *Atmosphere*, 2020, **11**, 636.

10 X. Shi and G. P. Brasseur, *Geophys. Res. Lett.*, 2020, **47**, e2020GL088070.

11 R. Zhang, Y. Zhang, H. Lin, X. Feng, T.-M. Fu and Y. Wang, *Atmosphere*, 2020, **11**, 433.

12 Q. Zhang, Y. Pan, Y. He, W. W. Walters, Q. Ni, X. Liu, G. Xu, J. Shao and C. Jiang, *Sci. Total Environ.*, 2021, **753**, 142238.

13 P. Wang, K. Chen, S. Zhu, P. Wang and H. Zhang, *Resour., Conserv. Recycl.*, 2020, **158**, 104814.

14 Y. Sun, L. Lei, W. Zhou, C. Chen, Y. He, J. Sun, Z. Li, W. Xu, Q. Wang, D. Ji, P. Fu, Z. Wang and D. R. Worsnop, *Sci. Total Environ.*, 2020, **742**, 140739.

15 S. Sharma, M. Zhang, Anshika, J. Gao, H. Zhang and S. H. Kota, *Sci. Total Environ.*, 2020, **728**, 138878.

16 I. De Smedt, G. Pinardi, C. Vigouroux, S. Compernolle, A. Bais, N. Benavent, F. Boersma, K. L. Chan, S. Donner, K. U. Eichmann, P. Hedelt, F. Hendrick, H. Irie, V. Kumar, J. C. Lambert, B. Langerock, C. Lerot, C. Liu, D. Loyola, A. Piters, A. Richter, C. Rivera Cárdenas, F. Romahn, R. G. Ryan, V. Sinha, N. Theys, J. Vlietinck, T. Wagner, T. Wang, H. Yu and M. Van Roozendael, *Atmos. Chem. Phys.*, 2021, **21**, 12561–12593.

17 T. Verhoelst, S. Compernolle, G. Pinardi, J. C. Lambert, H. J. Eskes, K. U. Eichmann, A. M. Fjæraa, J. Granville, S. Niemeijer, A. Cede, M. Tiefengraber, F. Hendrick, A. Pazmiño, A. Bais, A. Bazureau, K. F. Boersma, K. Bognar, A. Dehn, S. Donner, A. Elokhov, M. Gebetsberger, F. Goutail, M. Grutter de la Mora, A. Gruzdev, M. Gratsea, G. H. Hansen, H. Irie, N. Jepsen, Y. Kanaya, D. Karagkiozidis, R. Kivi, K. Kreher, P. F. Levelt, C. Liu, M. Müller, M. Navarro Comas, A. J. M. Piters, J. P. Pommereau, T. Portafaix, C. Prados-Roman, O. Puentedura, R. Querel, J. Remmers, A. Richter, J. Rimmer, C. Rivera Cárdenas, L. Saavedra de Miguel, V. P. Sinyakov, W. Stremme, K. Strong, M. Van Roozendael, J. P. Veefkind, T. Wagner, F. Wittrock, M. Yela González and C. Zehner, *Atmos. Meas. Tech.*, 2021, **14**, 481–510.

18 K. F. Boersma, H. J. Eskes, J. P. Veefkind, E. J. Brinksma, R. J. van der A, M. Sneep, G. H. J. van den Oord, P. F. Levelt, P. Stammes, J. F. Gleason and E. J. Bucsela, *Atmos. Chem. Phys.*, 2007, **7**, 2103–2118.

19 K. F. Boersma, H. J. Eskes, R. J. Dirksen, R. J. van der A, J. P. Veefkind, P. Stammes, V. Huijnen, Q. L. Kleipool, M. Sneep, J. Claas, J. Leitão, A. Richter, Y. Zhou and D. Brunner, *Atmos. Meas. Tech.*, 2011, **4**, 1905–1928.

20 S. Kato, F. G. Rose, S. H. Ham, D. A. Rutan, A. Radkevich, T. E. Caldwell, S. Sun-Mack, W. F. Miller and Y. Chen, *J. Geophys. Res.: Atmos.*, 2019, **124**, 1720–1740.

21 R. Xue, S. Wang, S. Zhang, S. He, J. Liu, A. Tanvir and B. Zhou, *Urban Clim.*, 2022, **43**, 101150.

22 S. Wu, B. Huang, J. Wang, L. He, Z. Wang, Z. Yan, X. Lao, F. Zhang, R. Liu and Z. Du, *Environ. Pollut.*, 2021, **273**, 116456.

23 C. Wang, T. Wang, P. Wang and W. Wang, *Remote Sens.*, 2022, **14**(1), 214.

24 China National Environmental Monitoring Center Network 2019, *China National Environmental Monitoring Distributor: Global Health Data Exchange (GHDx)*, Institute for Health Metrics and Evaluation, Seattle, WA, USA, 2020, <https://ghdx.healthdata.org/record/china-national-environmental-monitoring-center-network-2019>.

25 L. Kong, X. Tang, J. Zhu, Z. Wang, J. Li, H. Wu, Q. Wu, H. Chen, L. Zhu, W. Wang, B. Liu, Q. Wang, D. Chen, Y. Pan, T. Song, F. Li, H. Zheng, G. Jia, M. Lu, L. Wu and G. R. Carmichael, *Earth Syst. Sci. Data*, 2021, **13**, 529–570.

26 E. J. Dunlea, S. C. Herndon, D. D. Nelson, R. M. Volkamer, F. San Martini, P. M. Sheehy, M. S. Zahniser, J. H. Shorter, J. C. Wormhoudt, B. K. Lamb, E. J. Allwine, J. S. Gaffney, N. A. Marley, M. Grutter, C. Marquez, S. Blanco, B. Cardenas, A. Retama, C. R. Ramos Villegas, C. E. Kolb, L. T. Molina and M. J. Molina, *Atmos. Chem. Phys.*, 2007, **7**, 2691–2704.

27 J. Li, Y. Wang, R. Zhang, C. Smeltzer, A. Weinheimer, J. Herman, K. F. Boersma, E. A. Celarier, R. W. Long, J. J. Szykman, R. Delgado, A. M. Thompson, T. N. Knepp, L. N. Lamsal, S. J. Janz, M. G. Kowalewski, X. Liu and C. R. Nowlan, *Atmos. Chem. Phys.*, 2021, **21**, 11133–11160.

28 R. Zhang, Y. Wang, C. Smeltzer, H. Qu, W. Koshak and K. F. Boersma, *Atmos. Meas. Tech.*, 2018, **11**, 3955–3967.

29 F. A. Alkuwari, S. Guillas and Y. Wang, *Atmos. Environ.*, 2013, **81**, 1–10.

30 Y. Cheng, Y. Wang, Y. Zhang, G. Chen, J. H. Crawford, M. M. Kleb, G. S. Diskin and A. J. Weinheimer, *Geophys. Res. Lett.*, 2017, **44**, 7061–7068.

31 Y. Cheng, Y. Wang, Y. Zhang, J. H. Crawford, G. S. Diskin, A. J. Weinheimer and A. Fried, *J. Geophys. Res.: Atmos.*, 2018, **123**, 7642–7655.

32 D. Gu, Y. Wang, C. Smeltzer and Z. Liu, *Environ. Sci. Technol.*, 2013, **47**, 12912–12919.

33 D. Gu, Y. Wang, C. Smeltzer and K. F. Boersma, *J. Geophys. Res.: Atmos.*, 2014, **119**, 7732–7740.

34 Q. Yan, Y. Wang, Y. Cheng and J. Li, *Environ. Sci. Technol.*, 2021, **55**, 12852–12861.

35 H. Qu, Y. Wang, R. Zhang, X. Liu, L. G. Huey, S. Sjostedt, L. Zeng, K. Lu, Y. Wu, M. Shao, M. Hu, Z. Tan, H. Fuchs, S. Broch, A. Wahner, T. Zhu and Y. Zhang, *Environ. Sci. Technol.*, 2021, **55**, 13718–13727.

36 H. Hersbach, B. Bell, P. Berrisford, S. Hirahara, A. Horányi, J. Muñoz-Sabater, J. Nicolas, C. Peubey, R. Radu, D. Schepers, A. Simmons, C. Soci, S. Abdalla, X. Abellán,



G. Balsamo, P. Bechtold, G. Biavati, J. Bidlot, M. Bonavita, G. De Chiara, P. Dahlgren, D. Dee, M. Diamantakis, R. Dragani, J. Flemming, R. Forbes, M. Fuentes, A. Geer, L. Haimberger, S. Healy, R. J. Hogan, E. Hólm, M. Janisková, S. Keeley, P. Laloyaux, P. Lopez, C. Lupu, G. Radnoti, P. de Rosnay, I. Rozum, F. Vamborg, S. Villaume and J.-N. Thépaut, *Q. J. R. Meteorol. Soc.*, 2020, **146**, 1999–2049.

37 B. Zheng, J. Cheng, G. Geng, X. Wang, M. Li, Q. Shi, J. Qi, Y. Lei, Q. Zhang and K. He, *Sci. Bull.*, 2021, **66**, 612–620.

38 R. V. Martin, C. E. Sioris, K. Chance, T. B. Ryerson, T. H. Bertram, P. J. Wooldridge, R. C. Cohen, J. A. Neuman, A. Swanson and F. M. Flocke, *J. Geophys. Res.: Atmos.*, 2006, **111**(D15), DOI: [10.1029/2005JD006680](https://doi.org/10.1029/2005JD006680).

39 J. D. East, B. H. Henderson, S. L. Napelenok, S. N. Koplitz, G. Sarwar, R. Gilliam, A. Lenzen, D. Q. Tong, R. B. Pierce and F. Garcia-Menendez, *Atmos. Chem. Phys.*, 2022, **22**, 15981–16001.

40 T. Sekiya, K. Miyazaki, H. Eskes, K. Sudo, M. Takigawa and Y. Kanaya, *Atmos. Meas. Tech.*, 2022, **15**, 1703–1728.

41 J. Li and Y. Wang, *Atmos. Chem. Phys.*, 2019, **19**, 15339–15352.

42 C. Zhao and Y. Wang, *Geophys. Res. Lett.*, 2009, **36**(6), DOI: [10.1029/2008GL037123](https://doi.org/10.1029/2008GL037123).

43 D. Gu, Y. Wang, R. Yin, Y. Zhang and C. Smeltzer, *Atmos. Meas. Tech.*, 2016, **9**, 5193–5201.

44 A. H. Souri, C. R. Nowlan, G. González Abad, L. Zhu, D. R. Blake, A. Fried, A. J. Weinheimer, A. Wisthaler, J. H. Woo, Q. Zhang, C. E. Chan Miller, X. Liu and K. Chance, *Atmos. Chem. Phys.*, 2020, **20**, 9837–9854.

45 J. van Geffen, H. Eskes, S. Compernolle, G. Pinardi, T. Verhoelst, J. C. Lambert, M. Sneep, M. ter Linden, A. Ludewig, K. F. Boersma and J. P. Veefkind, *Atmos. Meas. Tech.*, 2022, **15**, 2037–2060.

46 Q. Yang, Y. Wang, C. Zhao, Z. Liu, W. I. Gustafson Jr. and M. Shao, *Environ. Sci. Technol.*, 2011, **45**, 6404–6410.

47 B. Zheng, Q. Zhang, G. Geng, C. Chen, Q. Shi, M. Cui, Y. Lei and K. He, *Earth Syst. Sci. Data*, 2021, **13**, 2895–2907.

48 F. Liu, A. Page, S. A. Strode, Y. Yoshida, S. Choi, B. Zheng, L. N. Lamsal, C. Li, N. A. Krotkov and H. Eskes, *Sci. Adv.*, 2020, **6**, eabc2992.

49 The Government of the People's Republic of China, *The Whole Nation is United and Helps Each Other—China's Vivid Practice of Fighting the Epidemic with Unity*, [https://www.gov.cn/xinwen/2020-04/25/content\\_5506182.htm](https://www.gov.cn/xinwen/2020-04/25/content_5506182.htm).

50 D. Li, Q. Wu, H. Wang, H. Xiao, Q. Xu, L. Wang, J. Feng, X. Yang, H. Cheng and L. Wang, *Atmos. Pollut. Res.*, 2021, **12**, 101232.

51 Z. Wang, I. Uno, K. Yumimoto, S. Itahashi, X. Chen, W. Yang and Z. Wang, *Atmos. Environ.*, 2021, **244**, 117972.

52 J. Ding, R. J. van der A, H. J. Eskes, B. Mijling, T. Stavrakou, J. H. G. M. van Geffen and J. P. Veefkind, *Geophys. Res. Lett.*, 2020, **47**, e2020GL089912.

53 Y. Tong, Y. Ma and H. Liu, *Acta Geogr. Sin.*, 2020, **75**, 2505–2520.

54 Y. Kuang, Z. Zou, X. Zhang and Y. Chang, *Acta Sci. Circumstantiae*, 2021, **41**, 1165–1172.

55 J. Hu, H. Xu, Y. Yao and L. Zheng, *China Remote Work from Home Development Report*, National School of Development at Peking University, 2022.

56 *Encourage and support enterprises to carry out online office, remote office and home office*, Cailian press, 2020, <https://www.cls.cn/detail/438597>.

57 Hangzhou Municipal People's Government, *The Hangzhou Municipal Committee of the Communist Party of China and the Hangzhou Municipal People's Government Issued a Number of Policies on Strictly Implementing Epidemic Prevention and Control to Help Enterprises Resume Work and Production*, [https://www.hangzhou.gov.cn/art/2020/2/11/art\\_1345197\\_41899719.html](https://www.hangzhou.gov.cn/art/2020/2/11/art_1345197_41899719.html).

58 N. Dandan, *Three Perspectives on the Lives of Shanghai People during the Epidemic*, <https://cn.weforum.org/stories/2020/03/san-ge-shi-jiao-kan-shang-hai-feng-cheng-hou-de-sheng-huo/>.

59 South China Morning Post, *China Coronavirus: At least Three Suspected Cases Found in Shenzhen, Shanghai, Sources Say*, <https://www.scmp.com/news/china/society/article/3046681/china-coronavirus-least-three-suspected-cases-found-shenzhen>.

60 T. L. He, D. B. A. Jones, K. Miyazaki, K. W. Bowman, Z. Jiang, X. Chen, R. Li, Y. Zhang and K. Li, *Atmos. Chem. Phys.*, 2022, **22**, 14059–14074.

61 S. Tan, S. Lai, F. Fang, Z. Cao, B. Sai, B. Song, B. Dai, S. Guo, C. Liu, M. Cai, T. Wang, M. Wang, J. Li, S. Chen, S. Qin, J. R. Floyd, Z. Cao, J. Tan, X. Sun, T. Zhou, W. Zhang, A. J. Tatem, P. Holme, X. Chen and X. Lu, *Natl. Sci. Rev.*, 2021, **8**(11), nwab148, DOI: [10.1093/nsr/nwab148](https://doi.org/10.1093/nsr/nwab148).

62 L. Jin, J. Chen, Z. Chen, X. Sun and B. Yu, *Transp. Policy*, 2022, **121**, 90–99.

63 Y. Gu, Y. Chen, X. Wang and Z. Chen, *Case Stud. Transp. Policy*, 2023, **12**, 101014.

64 S. Fei, R. A. Wagan, A. Hasnain, A. Hussain, U. A. Bhatti and E. Elahi, *Front. Environ. Sci.*, 2022, **10**, DOI: [10.3389/fenvs.2022.952310](https://doi.org/10.3389/fenvs.2022.952310).

65 Guangming Daily, *[Promoting High-Quality Development] Jiangsu: The Manufacturing Industry is Well Developed, Accounting for about 1/8 of the Country's Total*, 2025, <https://en.chinadaily.com.cn/a/202404/02/WS660bb82ba3109f7860dd800a.html>.

66 China Daily, *Jiangsu Ranks 1st in Key Economic Areas, according to Provincial Legislature Session*, [https://en.npc.gov.cn.cdurl.cn/2025-01/20/c\\_1065492.htm](https://en.npc.gov.cn.cdurl.cn/2025-01/20/c_1065492.htm).

67 Y. D. Wei and C. C. Fan, *Prof. Geogr.*, 2000, **52**, 455–469.

68 CHWANG, *Jiangsu Cross-border E-commerce Industry Belt Map Officially Released*, <https://www.chwang.com/article/182433633074>.

69 J. Xia, *In-depth Report on the Cross-border E-commerce Industry: China's Cross-border E-commerce Industry Upgrades, and the "Four Little Dragons" Sound the Rally Call to Go Overseas*, China Merchants Bank Institute, China Merchants Bank Institute, 2024.

70 Q. Zhou, *China's Most Productive Provinces and Cities as per 2021 GDP Statistics*, <https://www.china-briefing.com/news/>

[chinas-2021-gdp-performance-a-look-at-major-provinces-and-cities/](https://doi.org/10.1039/DATM00014A).

71 The Observatory of Economic Complexity, *Jiangsu Province Historical Data*, [https://oec.world/en/profile/subnational\\_chn/jiangsu-province#bespoke-title-1342](https://oec.world/en/profile/subnational_chn/jiangsu-province#bespoke-title-1342).

72 Q. Xinzong, *Econ. Res.*, 2022, **35**, 1526–1541.

73 Q. Dai, L. Hou, B. Liu, Y. Zhang, C. Song, Z. Shi, P. K. Hopke and Y. Feng, *Geophys. Res. Lett.*, 2021, **48**, e2021GL093403.

74 The State Council of the People's Republic of China, *The Central Guidance Group went to Huanggang, Hubei to Guide the Implementation of Prevention and Control Measures such as “Collect all that should be Collected”*, [https://www.gov.cn/guowuyuan/2020-02/10/content\\_5476641.htm](https://www.gov.cn/guowuyuan/2020-02/10/content_5476641.htm).

75 Huanggang City Novel Coronavirus Pneumonia Epidemic Prevention and Control Command Center, *Announcement from Huanggang City COVID-19 Prevention and Control Headquarters*, <https://ncp.pkulaw.com/epidemiclaw/9082eb8d5a65550627e509ebbeadd782bdfb.html>.

76 Xinhua Net, *Drawing a Bright “Volunteer Red”—Sketch of the Group of Volunteers for Epidemic Prevention and Control in Huanggang, Hubei*, [http://www.xinhuanet.com/politics/2020-03/17/c\\_1125723341.htm](http://www.xinhuanet.com/politics/2020-03/17/c_1125723341.htm).

77 Wuhan Municipal Health Commission, *Wuhan Starts Building Three “Square Cabin Hospitals” Overnight*, [https://wjw.wuhan.gov.cn/ztzl\\_28/fk/fkdt/202004/t20200430\\_1196705.shtml](https://wjw.wuhan.gov.cn/ztzl_28/fk/fkdt/202004/t20200430_1196705.shtml), accessed 30 April 2025.

78 Central People's Government of the People's Republic of China, *Rushing to Build a “Life Ark” – Central Enterprises Rush to Help Build Wuhan Fangcang Hospital*, [https://www.gov.cn/xinwen/2020-02/23/content\\_5482450.htm](https://www.gov.cn/xinwen/2020-02/23/content_5482450.htm), accessed 30 April 2025.

79 X. Zhang and L. Xu, *“Administrative Freeze” Reappears, How Can Counterpart Assistance “Fight the Epidemic”?*, <https://cn.ifpri.org/archives/6404>.

80 Nanchang Municipal People's Government, *The Most Beautiful People Going against the Flow in Nanchang, their Stories are Moving!*, <https://www.nc.gov.cn/ncszf/yqfk/202001/91d7aab5d27c42be9ad915349c5b1c9d.shtml>.

81 Xinhua Net, *Hefei: More than 300 tons of Fresh Vegetables Rush to Wuhan*, 2025, [https://www.gov.cn/xinwen/2020-01-30/content\\_5473184.htm#1](https://www.gov.cn/xinwen/2020-01-30/content_5473184.htm#1), accessed 03 May 2025.

82 Q. Cui, L. He, Y. Liu, Y. Zheng, W. Wei, B. Yang and M. Zhou, *Transp. Policy*, 2021, **103**, 103–115.

83 I. Twinn, N. Qureshi, M. López Conde, C. Garzón Guinea and D. Perea Rojas, *The Impact of COVID-19 on Logistics*, International Finance Corporation, World Bank Group, 2020.

84 Z. Cui, X. Fu, J. Wang, Y. Qiang, Y. Jiang and Z. Long, *Transp. Policy*, 2022, **120**, 11–22.

85 S. Wei and L. Wang, *Humanit. Soc. Sci. Commun.*, 2020, **7**, 145.

86 X. Lu, J. Tan, Z. Cao, Y. Xiong, S. Qin, T. Wang, C. Liu, S. Huang, W. Zhang, L. B. Marczak, S. I. Hay, L. Thabane, G. H. Guyatt and X. Sun, *Health Data Sci.*, 2021, **2021**, 9796431.

87 Y. Liu, Z. Wang, B. Rader, B. Li, C.-H. Wu, J. D. Whittington, P. Zheng, N. C. Stenseth, O. N. Bjornstad, J. S. Brownstein and H. Tian, *Lancet Digital Health*, 2021, **3**, e349–e359.

88 H. Fang, L. Wang and Y. Yang, *J. Publ. Econ.*, 2020, **191**, 104272.

89 M. U. G. Kraemer, C.-H. Yang, B. Gutierrez, C.-H. Wu, B. Klein, D. M. Pigott, Open COVID-19 Data Working Group, L. du Plessis, N. R. Faria, R. Li, W. P. Hanage, J. S. Brownstein, M. Layen, A. Vespignani, H. Tian, C. Dye, O. G. Pybus and S. V. Scarpino, *Science*, 2020, **368**, 493–497.

90 J. Xia, T. Li, Z. Yu, E. Chen, Y. Yue, Z. Li and Y. Zhou, *Geospatial Inf. Sci.*, 2023, **26**, 627–641.

91 K. J. Tu, *COVID-19 Pandemic's Impacts on China's Energy Sector: A Preliminary Analysis*, Center on Global Energy Policy, Columbia University, 2020.

92 M. Zhao, Y. Niu, L. Tian, Y. Liu and Q. Zhai, *Int. J. Environ. Res. Public Health*, 2021, **18**, 9736.

93 M. S. Mastoi, H. M. Munir, S. Zhuang, M. Hassan, M. Usman, A. Alahmadi and B. Alamri, *Int. J. Environ. Res. Public Health*, 2022, **19**, 4608.

94 International Energy Agency, *COVID-19 Impact on Electricity*, IEA, Paris, 2021.

95 N. Deng, B. Wang, Y. Qiu, J. Liu, H. Shi, B. Zhang and Z. Wang, *Energy Econ.*, 2022, **114**, 106318.

96 J. Ding, R. J. van der A, H. J. Eskes, B. Mijling, T. Stavrakou, J. Van Geffen and J. P. Veefkind, *Geophys. Res. Lett.*, 2020, **47**, e2020GL089912.

97 S. Feng, F. Jiang, H. Wang, H. Wang, W. Ju, Y. Shen, Y. Zheng, Z. Wu and A. Ding, *Geophys. Res. Lett.*, 2020, **47**, e2020GL090080.

